

# Excitatory Microcircuits within Superficial Layers of the Medial Entorhinal Cortex

Jochen Winterer,<sup>1,9,10</sup> Nikolaus Maier,<sup>1,9</sup> Christian Wozny,<sup>1,2</sup> Prateep Beed,<sup>1,3</sup> Jörg Breustedt,<sup>1</sup> Roberta Evangelista,<sup>4,5</sup> Yangfan Peng,<sup>6</sup> Tiziano D'Albis,<sup>4,5</sup> Richard Kempter,<sup>4,5</sup> and Dietmar Schmitz<sup>1,3,4,7,8,11,\*</sup>

<sup>1</sup>Neuroscience Research Center, Charité-Universitätsmedizin Berlin, 10117 Berlin, Germany

<sup>2</sup>Strathclyde Institute of Pharmacy and Biomedical Sciences, University of Strathclyde, Glasgow G4 0RE, UK

<sup>3</sup>Berlin Institute of Health, 10117 Berlin, Germany

<sup>4</sup>Bernstein Center for Computational Neuroscience Berlin, 10115 Berlin, Germany

<sup>5</sup>Department of Biology, Institute for Theoretical Biology, Humboldt-Universität zu Berlin, 10115 Berlin, Germany

<sup>6</sup>Institute of Neurophysiology, Charité-Universitätsmedizin Berlin, 10117 Berlin, Germany

<sup>7</sup>Cluster of Excellence NeuroCure, 10117 Berlin, Germany

<sup>8</sup>Center for Neurodegenerative Diseases Berlin, 10117 Berlin, Germany

<sup>9</sup>These authors contributed equally

<sup>10</sup>Present address: Brain Research Institute, University of Zürich, 8057 Zürich, Switzerland

<sup>11</sup>Lead Contact

\*Correspondence: [dietmar.schmitz@charite.de](mailto:dietmar.schmitz@charite.de)

<http://dx.doi.org/10.1016/j.celrep.2017.04.041>

## SUMMARY

The distinctive firing pattern of grid cells in the medial entorhinal cortex (MEC) supports its role in the representation of space. It is widely believed that the hexagonal firing field of grid cells emerges from neural dynamics that depend on the local microcircuitry. However, local networks within the MEC are still not sufficiently characterized. Here, applying up to eight simultaneous whole-cell recordings in acute brain slices, we demonstrate the existence of unitary excitatory connections between principal neurons in the superficial layers of the MEC. In particular, we find prevalent feed-forward excitation from pyramidal neurons in layer III and layer II onto stellate cells in layer II, which might contribute to the generation or the inheritance of grid cell patterns.

## INTRODUCTION

The hippocampus and parahippocampal regions are critically involved in learning and memory as well as in neurological diseases such as temporal lobe epilepsy and Alzheimer's disease. More specifically, these regions are engaged in neuronal computations representing space. In particular, neurons in the medial entorhinal cortex (MEC) show grid field activity in which firing locations are organized in a regular hexagonal lattice (Fyhn et al., 2004; Hafting et al., 2005; Moser et al., 2014; Rowland et al., 2016). The mechanisms underlying the formation of grid fields are still unclear and an ongoing matter of intense debate (McNaughton et al., 2006; Fuhs and Touretzky, 2006; Burgess et al., 2007; Burak and Fiete, 2009). It has been proposed that pattern formation in grid cell activity could arise via Turing instability (McNaughton et al., 2006; Kropff and Treves, 2008; Row-

land et al., 2016), where competition between short-range activation and long-range suppression generates stable spatial patterns (Turing, 1952). Long-range suppression could be due to recurrent inhibitory projections, as proposed by attractor models (McNaughton et al., 2006; Fuhs and Touretzky, 2006; Burak and Fiete, 2009), or due to firing rate adaptation, as proposed by adaptation models (Kropff and Treves, 2008; Bailu et al., 2012). Although based on the same principle, these two model classes rely on very different neuronal implementations and make specific predictions about the synaptic connectivity and single-cell properties within the MEC. However, experimental evidence for both scenarios is rare or even contradictory (Beed et al., 2010; Couey et al., 2013; Buetfering et al., 2014). Therefore, a fundamental step to unveiling the origin of grid cell patterns is to characterize the local microcircuits within the superficial layers of the MEC.

Here we report on feedforward and recurrent excitatory connections among principal cells of the MEC. In an *in vitro* slice preparation, we performed simultaneous whole-cell patch-clamp recordings of up to eight neurons in layers II and III of the rat MEC. Such octuple recordings offer a combinatorial advantage over dual or quadruple recordings in that up to 56 connections can be tested at once, thereby facilitating connectivity studies even when the connectivity rate is low. Synaptic coupling was tested by driving presynaptic action potential firing with somatic current injections, leading to excitatory postsynaptic potentials (EPSPs) in the case of synaptic coupling. With this technique, we analyzed the connection probability and synaptic properties in the superficial layers of the MEC.

## RESULTS

### Local Excitatory Connections of Layer III Pyramidal Cells

Within the MEC—or cortical subfields in general—synaptic connections between principal neurons can be separated into

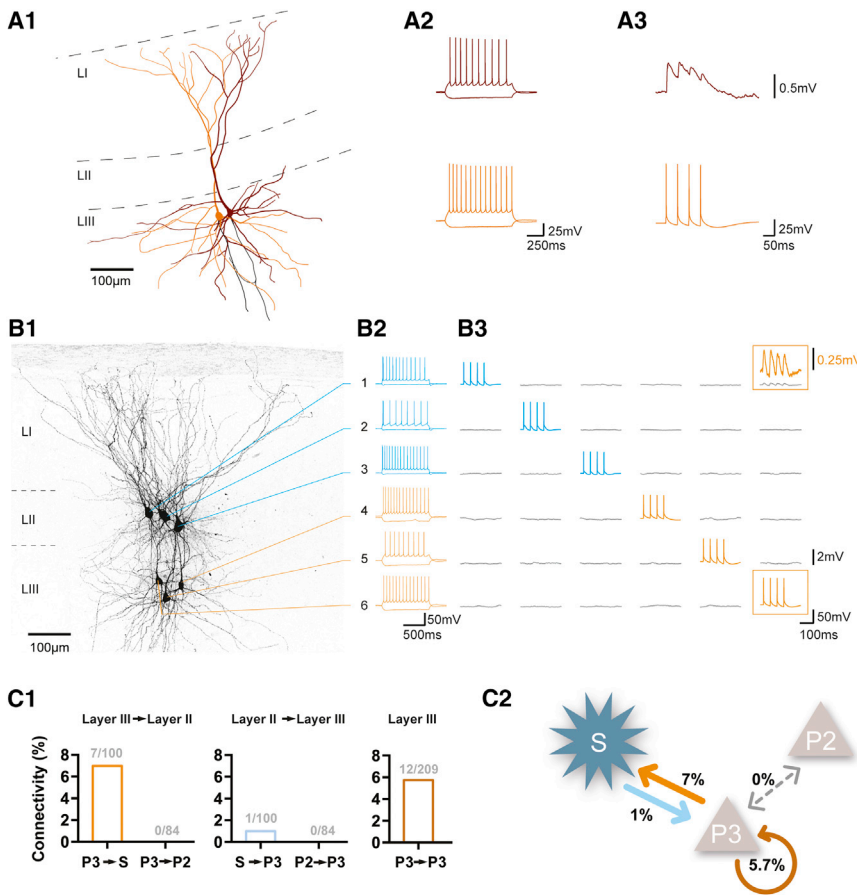


**Figure 1. Inter- and Intra-laminar Excitatory Connectivity in Superficial Layers of the MEC**

(A1) Reconstruction of two layer III pyramidal cells. (A2) Firing patterns of the recorded cells. (A3) Presynaptic action potentials and corresponding EPSPs.

(B1) Biocytin staining of six simultaneously recorded cells. All cells are numbered according to the labels shown on the right. Three principal neurons were recorded in layer II of the MEC (blue lines), and three pyramidal cells were recorded in layer III (orange lines).

(B2) Firing patterns of the recorded cells.

(B3) One neuron was stimulated with a train of four action potentials while the postsynaptic responses of the other neurons were monitored. Data were recorded in current clamp mode and are displayed in the corresponding columns for pre- and postsynaptic signals. Presynaptic action potentials of pyramidal cell 6 (orange box, bottom) elicited EPSPs in the connected stellate cell 1 (orange box, top; orange trace, magnification).

(C1) Connection probability of contacts from layer III onto layer II (left), from layer II onto layer III (center), and from intra-laminar contacts within layer III, determined by the number of connected pairs divided by the number of tested connections. (C2) Connectivity scheme of layer III pyramidal cells, stellate cells, and layer II pyramidal cells in superficial layers of the MEC.

P2 and P3, pyramidal cell in layer II or III, respectively; S, stellate cell; LI, layer I; LII, layer II; LIII, layer III.

intra- and inter-laminar connections. To date, there are only a few reports published addressing the neuronal connectivity in the MEC (Dhillon and Jones, 2000; Beed et al., 2010; Couey et al., 2013; Fuchs et al., 2016). Motivated by these, we first tested the intra-laminar connectivity among identified principal neurons in layer III of the MEC. Confirming an earlier report that had been performed using sharp microelectrodes in a “blind” approach (Dhillon and Jones, 2000), we found that layer III pyramidal neurons contact other pyramidal neurons in this layer at a connectivity rate of 5.7% (Figures 1A1–1A3, 12 of 209 connections tested; Figures 1C1 and 1C2). Next, we were interested in the inter-laminar connectivity between superficial layers II and III (Figures 1B1–1B3). We observed excitatory connections from layer III pyramidal neurons onto layer II principal neurons at a rate of 3.8% (7 of 184 connections tested, ignoring possible differences in cell types of target cells in layer II). In turn, we found only one excitatory connection projecting from a layer II principal neuron onto a pyramidal cell in layer III (0.5%, 1 of 184 connections tested). These findings suggest a directionality of connections arising from layer III pyramidal neurons onto layer II principal neurons.

### Cell Type-Specific Feedforward Connectivity

In contrast to layer III, where the majority of neurons are pyramidal cells, principal neurons in layer II comprise two well described classes of cells: stellate cells and pyramidal cells

(Varga et al., 2010). To characterize and discriminate these two cell types of layer II, we combined immunoreactivity against reelin or calbindin with an analysis of intrinsic electrophysiological properties. Reelin- and calbindin-expressing principal neurons were classified as stellate cells and pyramidal cells, respectively (Figure 2). We confirmed earlier findings (Varga et al., 2010; Fuchs et al., 2016) showing that these two cell types represent electrophysiologically distinct groups (Figure S1). Importantly, we identified one intrinsic parameter as a particularly reliable measure to discriminate reelin- and calbindin-expressing neurons: the depolarizing “sag” potential analyzed in response to hyperpolarizing voltage steps was significantly shorter in reelin-positive cells compared with calbindin-expressing cells (reelin-positive cells ( $n = 110$ ,  $31.3 \pm 3.7$  ms) versus calbindin-positive cells ( $n = 25$ ,  $45.9 \pm 7.4$  ms); Figure S1). Therefore, we used this cellular property to unequivocally classify principal neurons in layer II for which the immunoreactivity was uncertain (see also Figure S1 and cell classification in the Supplemental Experimental Procedures). We applied these criteria and found that inter-laminar excitatory synaptic contacts are cell type-specific; i.e., all observed contacts were between pyramidal neurons in layer III and stellate cells in layer II. However, in these recordings, we did not detect any inter-laminar connection among pyramidal neurons of both layers (0 of 84 connections tested for each condition; Figures 1C1 and 1C2). Remarkably,

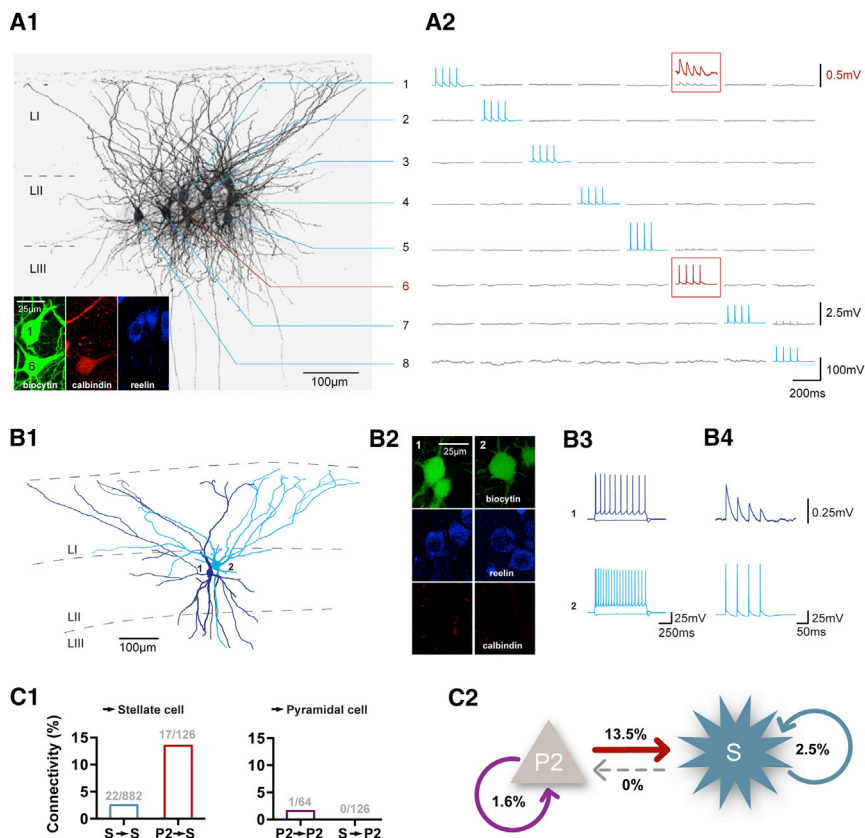


**Figure 2. Stellate Cells, but Not Pyramidal Neurons, Receive Strong Excitatory Input in Layer II of the MEC**

(A1) Biocytin staining of eight simultaneously recorded neurons. All cells are numbered according to the labels shown on the right. The inset shows the immunohistochemistry of cells 1 and 6. The upper cell (1) is immunoreactive to reelin but not to calbindin, whereas cell 6 is immunoreactive to calbindin but not to reelin.

(A2) One neuron was stimulated with a train of four action potentials while the postsynaptic responses of the other neurons were monitored. Data were recorded in current clamp mode and are displayed in the corresponding columns for pre- and postsynaptic signals. The presynaptic action potentials of cell 6 (red box) elicited EPSPs in the connected cell 1 (red trace on top, magnification).

(B1) Reconstruction of two layer II stellate cells. (B2) Immunohistochemistry of biocytin-filled, reelin-positive, calbindin-negative cells in layer II of the MEC.

(B3) Firing patterns of the recorded cells. (B4) Presynaptic action potentials of cell 2 and corresponding postsynaptic EPSPs in cell 1.

(C1) Connection probability of contacts onto stellate cells (left) and layer II pyramidal cells (right), as determined by the number of connected pairs divided by the number of tested connections.

(C2) Connectivity scheme of layer II pyramidal cells and stellate cells in layer II of the MEC.

we observed layer III pyramidal neurons to contact layer II stellate cells at a rate of 7.0% (7 of 100 tested connections; [Figures 1C1 and 1C2](#)). In contrast, we found only one connection from layer II stellate cells onto layer III pyramidal cells (1.0%, 1 of 100 connections tested; [Figures 1C1 and 1C2](#)). Intrinsic electrophysiological parameters—i.e., the ratio of the first two interspike intervals (ISIs) upon injection of positive current (ISI 1 / ISI 2, index for burst firing), the latency to the first spike, and the depolarizing afterpotential (dAP)—were recently used to further categorize principal neurons in layer II of the MEC ([Fuchs et al., 2016](#)). However, in our hands, the same analysis did not unveil additional clusters of principal neurons in layer II of the MEC ([Figures S1 and S2](#)).

Together, our multi-cellular recordings demonstrate connections among principal neurons in the superficial layers II and III of the MEC; these connections are cell type-specific and largely unidirectional toward stellate cells of layer II.

### Excitatory Synaptic Connectivity within Layer II

Having established the presence of predominantly unidirectional coupling that connects layers III and II, we were interested in the excitatory connectivity within layer II of the MEC ([Figures 2A and 2B](#)). We tested a total of 882 synaptic connections and found 22 excitatory connections among stellate cells (connectivity, ~2.5%; [Figures 2C1 and 2C2](#)). Again, we observed that connections between the two principal neuron entities exhibit a cell type-specific wiring scheme. Although pyramidal cells form syn-

aptic contacts onto stellate cells at a remarkable rate of ~13.5% (17 of 126 tested connections; [Figure 2C](#)), stellate cells never contact pyramidal neurons (0 of 126 connections tested; [Figure 2C](#)). Taken together, these results suggest a specific directionality in the information flow within the superficial layers of the MEC, with a majority of the excitatory projections converging onto stellate cells in layer II.

### Characteristics of Excitatory Connections in the Superficial Layers of the MEC

Finally, we analyzed various properties of synaptic transmission in the coupled cell pairs and observed specific differences. First, we found significantly higher amplitudes of unitary synaptic responses at contacts of layer II pyramids onto layer II stellate cells (range, from 0.09 to 4.6 mV; median, 0.3 mV; interquartile range [IQR], 0.7 mV; [Figure 3A](#)) compared with unitary synaptic connections among stellate cells (range, from 0.07 to 0.9 mV; median, 0.15 mV; IQR, 0.13 mV; [Figure 3A](#);  $p = 0.01$ ). Second, intra-laminar connections onto stellate cells had particularly short synaptic delays compared with inter-laminar projections and layer III-layer III connections (latency,  $p < 0.001$ ; [Figure 3B](#); for further analyses on action potential (AP) time to peak values, distance distribution, and age dependence of excitatory connectivity, see [Figures S3B–S3D](#)). Third, we observed that the EPSP kinetics of intra-laminar connections onto stellate cells were particularly fast in comparison with layer III-layer II or layer III-layer III connections (rise time (10%–90%) and half-width of

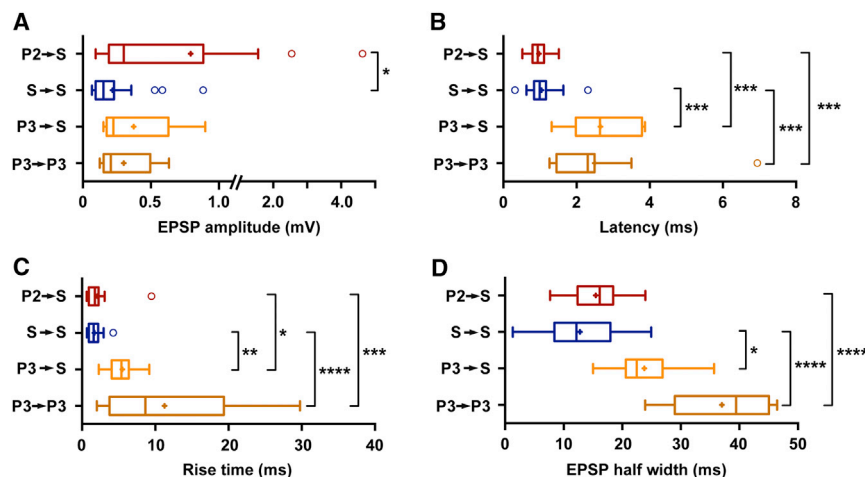


**Figure 3. Properties of Excitatory Synaptic Connections in the Superficial Layers of the MEC**

(A) EPSP amplitudes. For each spike train, the first EPSP amplitude was analyzed. All recordings were done at  $-60$  mV.  
 (B) Synaptic delays as determined by the time from the peak of the presynaptic AP to the onset of the EPSPs.  
 (C) Rise times (10%–90%) of the EPSPs.  
 (D) Half-width of the EPSPs.  
 The statistical significance of the displayed differences was assessed by Dunn's test of multiple comparisons. \* $p \leq 0.05$ , \*\* $p \leq 0.01$ , \*\*\* $p \leq 0.001$ , \*\*\*\* $p \leq 0.0001$ .

EPSP; Figures 3C and 3D). To characterize the strength of the coupling of different cell types (Figure 4A), we weighted the connectivity rates by EPSP amplitudes (Figure 4B), which allowed to compare more directly the relative strengths of the different synaptic junctions. Intriguingly, we found that the total weighted feedforward connectivity onto stellate cells was much stronger compared with the recurrent connectivity among these neurons, even in light of the ratio of 60%:40% reported for reelin-positive stellate cells and calbindin-positive (or Wolfram syndrome 1-positive) pyramidal cells (Varga et al., 2010; Sun et al., 2015). This directionality within the superficial layers of the MEC suggests organizational principles in a brain area that is regarded to be pivotal for memory formation.

## DISCUSSION

The present study provides direct evidence for feedforward and recurrent excitatory connectivity within the superficial layers of the MEC. Remarkably, we demonstrate a high rate of feedforward excitatory connections from pyramids of layers III and II onto stellate cells in layer II (Figure 4A). In addition, we observe a high synaptic coupling strength at the pyramidal cell-stellate cell synapse within layer II. We also consistently find recurrent excitatory synaptic connections among pyramidal cells in layer III and stellate cells in layer II. This latter result challenges the prevailing view of excitatory connections among stellate cells in layer II of the MEC being sparse or even absent (Couey et al., 2013; Pastoll et al., 2013; Fuchs et al., 2016; for a comparison of connectivity values in the MEC, see Figure S3E). Although Fuchs et al. (2016) report on excitatory connections among intermediate stellate and stellate cells, our analysis does not support any additional differentiation. However, the reported connection probability of all stellate cells, irrespective of their sub-classification, resembles the connectivity rate we observe in our present study. In addition, similar to our findings, the highest connectivity rate in layer II was found in connections impinging on stellate cells (Fuchs et al., 2016). Nonetheless, the origin of the differences in the classification of principal neurons in layer II remains unclear.

The observed excitatory couplings are consistent with cross-correlation analysis of the spiking activity of MEC principal

neurons and grid cells in behaving rats (Quilichini et al., 2010; Tocker et al., 2015) and with an increase in excitatory synaptic transmission during grid field crossing (Schmidt-Hieber and Häusser, 2013; Domnisoru et al., 2013; Heys et al., 2014).

From a functional perspective, our data suggest that mono-synaptic recurrent excitatory connections could constrain grid cell activity within a low-dimensional continuous attractor (Yoon et al., 2013). This may explain why grid cells of the same module tend to react in concert to external manipulations of the geometry of the environment (Barry et al., 2007, 2012) or to manipulations of the light conditions (Chen et al., 2016; Pérez-Escobar et al., 2016). However, it remains unclear whether such recurrent connections are also responsible for the formation of grid cell patterns (McNaughton et al., 2006; Fuhs and Touretzky, 2006; Burak and Fiete, 2009). We found that the feedforward connectivity onto layer II stellate cells is much stronger compared with the recurrent connectivity among these neurons (Figure 4B). Therefore, assuming that grid cell patterns do originate in layer II stellate cells, where most of the excitatory inputs converge (Figure 4B), our data support feedforward rather than recurrent dynamics shaping grid cell activity in this region. This view favors feedforward models of grid cell formation (Kropff and Treves, 2008; Bailu et al., 2012). Alternatively, layer II stellate cells could inherit their grid-like tuning from upstream principal cell populations, such as pyramidal cells in layer II (Sun et al., 2015) or layer III, rather than generating spatial patterns exclusively. This inheritance process, which requires a specific functional connectivity pattern, could be achieved in an unsupervised manner and could result in improved grid-like tuning in the downstream structure. Indeed, we have modeled such a scenario and found that the activity of grid cells might be inherited and improved by a Hebbian mechanism (Figure S4). Future studies will have to examine this scenario using state-of-the-art genetic cell type-specific manipulations in detail. Importantly, recent work has already provided some evidence for grid cells being present in adjacent brain regions, such as the pre- and parasubiculum (Boccaro et al., 2010).

We obtained our data from acute brain slice preparation. This approach has two consequences: First, because of the slicing,

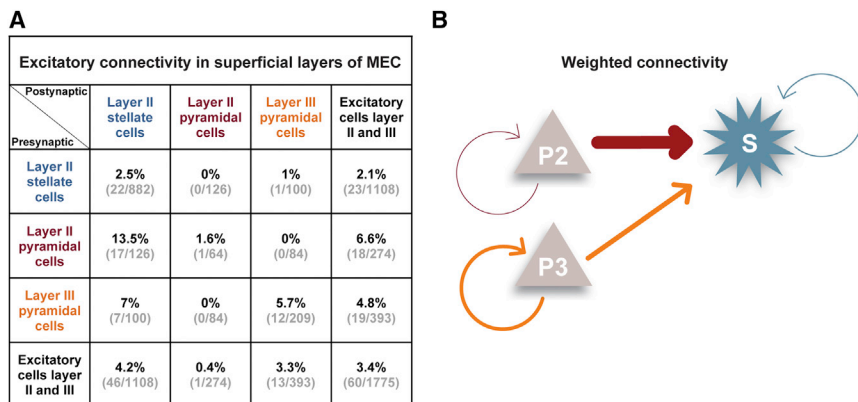


**Figure 4. Comparison of Connectivity Rates Demonstrates Substantial Feedforward Excitatory Signaling onto Layer II Stellate Cells**

(A) Contingency table of the excitatory connectivity in superficial layers of the MEC. Displayed are the connectivity rate and the observed and tested connections (in brackets).

(B) Connectivity scheme with weighted excitatory synaptic connections to indicate the relative strengths of the investigated synaptic connections. The strokes of the arrows reflect the connection probabilities multiplied by the medians of the amplitudes of the EPSPs (in a.u.): P2 → S, 4.1; P3 → S, 1.6; S → S, 0.4; P3 → P3, 1.2; P2 → P2, 0.3. Together, these values highlight a feedforward signaling onto layer II stellate cells of the MEC.

axons are cut, most likely not in a uniform way, and all cell sub-type-specific connections are severed equally; in contrast, because of the geometrical layout of cortical structures, the connections between different subsets of neurons might be affected differently (Barth et al., 2016). As a consequence, our data may provide an underestimation of the actual excitatory connectivity matrix in superficial layers of the MEC; however, recent work using two-photon targeted whole-cell recordings in vivo surprisingly found very similar connectivity rates as in slice preparations (Jouhanneau et al., 2015). Second, by its nature, our approach precludes the investigation of grid cell firing. However, grid field activity is evident in principal cells of superficial layers of the MEC (Rowland et al., 2016 but see Tang et al., 2015), and thus it is highly likely that the architecture of this microcircuit is the substrate that shapes this distinct pattern of activity.

In summary, our data highlight the presence of frequent excitatory synaptic connections among principal cells in the MEC and support the view that grid-forming neuronal networks can rely on excitatory connections.

## EXPERIMENTAL PROCEDURES

### Experimental Animals

Animal maintenance and experiments were in accordance with the respective guidelines of local authorities (Berlin state government, T0073/04) and followed the German Animal Welfare Act and European Council Directive 2010/63/EU regarding the protection of animals used for experimental and other scientific purposes.

### Electrophysiology

#### Slice Preparation

Wistar rats (post-natal day [P]21–P60, both sexes) were decapitated following isoflurane anesthesia. The brains were removed and transferred to ice-cold sucrose-based artificial cerebrospinal fluid (sACSF) containing 87 mM NaCl, 75 mM sucrose, 26 mM NaHCO<sub>3</sub>, 2.5 mM KCl, 1.25 mM NaH<sub>2</sub>PO<sub>4</sub>, 0.5 mM CaCl<sub>2</sub>, 7.0 mM MgCl<sub>2</sub>, and 25 mM glucose, saturated with 95% O<sub>2</sub> and 5% CO<sub>2</sub> (pH 7.4). Slices (400 μm, taken from the dorsal third of the MEC) were cut on a vibratome (VT1200S, Leica Biosystems) in a horizontal plane that was tilted to the perpendicular axis of the pial surface of the entorhinal cortex. Slices were stored in an interface chamber (32°C–34°C), continuously oxygenized with carbogen, and perfused with ACSF containing 119 mM NaCl, 26 mM NaHCO<sub>3</sub>, 10 mM glucose, 2.5 mM KCl, 2.5 mM CaCl<sub>2</sub>, 1.3 mM MgCl<sub>2</sub>, and 1.0 mM NaH<sub>2</sub>PO<sub>4</sub> at a rate of ~1 mL/min. The slices were allowed to recover for at least 1 hr after preparation before they were transferred into the recording chamber.

### Connectivity

As described recently (Böhm et al., 2015; Peng et al., 2017), recordings were performed in ACSF at 32°C–34°C in a submerged recording chamber. Cells in the MEC were identified using infrared differential contrast video microscopy (BX51WI, Olympus) and selected within a distance of 10–250 μm. We performed somatic whole-cell patch-clamp recordings (pipette resistance, 2.5–4 MΩ) of up to eight cells simultaneously. One cell was stimulated with a train of four action potentials at 50 Hz, elicited by 1- to 2-ms-long current injections of 2–4 nA. For characterization, increasing steps of current were injected (1 s; increment, 50 pA). In a few experiments, a hyperpolarizing or depolarizing holding current was applied to keep the membrane potential at –60 mV. In total, we recorded 136 layer III pyramidal cells, 87 layer II pyramidal cells, and 315 layer II stellate cells. The intracellular solution contained 135 mM potassium-gluconate, 6.0 mM KCl, 2.0 mM MgCl<sub>2</sub>, 0.2 mM EGTA, 5.0 mM Na<sub>2</sub>-phosphocreatine, 2.0 mM Na<sub>2</sub>-ATP, 0.5 mM Na<sub>2</sub>-GTP, 10 mM 4-(2-hydroxyethyl)-1-piperazineethanesulfonic acid (HEPES) buffer, and 0.2% biocytin. The pH level was adjusted to 7.2 with potassium hydroxide (KOH). Recordings were performed using Multiclamp 700A/B amplifiers (Molecular Devices). Signals were filtered at 6 kHz, sampled at 20 kHz, and digitized at 16-bit resolution using Digidata 1550 and pClamp 10 (Molecular Devices).

### Data Analysis

#### Connectivity

Synaptic connections were identified when there was a postsynaptic potential corresponding to the presynaptic stimulation in the averaged trace from 40–50 sweeps. A baseline period (2 ms) just prior to the stimulation and the averaged postsynaptic peak during the first action potential was used for the analysis of the EPSP amplitudes, synaptic delays, and EPSP kinetics with AxoGraph X (<https://axographx.com>). Only pairs in which the first postsynaptic peak was clearly discernible were used for analysis. The statistical significance of differences in EPSP amplitudes, latency, rise time, AP time to peak, half-width, or paired-pulse ratio (PPR) was calculated using Kruskal-Wallis test and post hoc Dunn's test for multiple comparisons. The example traces in Figures 1 and 2 were filtered at 1 kHz and represent averages of 25–50 sweeps. The AP trains in Figures 1B3 and 2A2 are displayed as single sweeps.

#### Immunohistochemistry and Neuroanatomy of Principal Cells

After recording, slices were transferred into a fixative solution containing 4% paraformaldehyde in 0.1 M phosphate buffer. Primary antibodies were diluted in incubation medium (PBS containing 2.5% normal goat serum and 1% Triton). Immunoreactions for calbindin were carried out with a rabbit antibody (Cb-38, Swant, diluted 1:10,000) and for reelin with a mouse antibody (MAB5354, Millipore, diluted 1:1,000). Secondary antibodies conjugated to Alexa 555 (or Alexa 594) and Alexa 647 (diluted 1:500, Molecular Probes) raised against mouse and rabbit were used to detect the location of the primary antibodies; streptavidin was conjugated to Alexa 488 for biocytin (diluted 1:500). The slices were then mounted in Fluoroshield (Sigma-Aldrich) and analyzed. Image stacks of specimens were imaged on a Leica TCS SP5 confocal microscope (Leica Microsystems). Images were quantified

using ImageJ software (<https://rsbweb.nih.gov/ij/>). The reconstructions in Figures 1B1 and 2A1 were done after blind deconvolution with AutoQuant X3 (MediaCybernetics). Figures 1A1 and 2B1 were done with the aid of the NeuroLucida 3D reconstruction system (MicroBrightField).

#### Cell Classification

For cell classification of layer II principal neurons, we made use of the differential immunoreactivity of these cells to reelin and calbindin and the analysis of intrinsic electrophysiological properties. For further details, see Supplemental Experimental Procedures.

#### SUPPLEMENTAL INFORMATION

Supplemental Information includes Supplemental Experimental Procedures and four figures and can be found with this article online at <http://dx.doi.org/10.1016/j.celrep.2017.04.041>.

#### AUTHOR CONTRIBUTIONS

The study was conceived and designed by D.S. and R.K. The electrophysiological experiments were performed by J.W., N.M., C.W., and P.B. J.W., R.E., N.M., C.W., P.B., and Y.P. analyzed the electrophysiological experiments. J.W. and J.B. analyzed the immunohistochemistry and neuroanatomy. T.D. and R.K. performed the modeling. J.W., N.M., D.S., T.D., and R.K. wrote the paper with help from C.W., P.B., and J.B.

#### ACKNOWLEDGMENTS

This study was supported by grants from the DFG (SFB 958, Exc 257, and KE 788/3-1), the Bernstein Center for Computational Neuroscience Berlin (01GQ1001A), Bernstein Focus Learning (01GQ0972), and BMBF (SMARTAGE) and a BIH Delbrück fellowship. The authors thank Susanne Rieckmann, Anke Schönherr, and Lisa Züchner for excellent technical assistance. We are indebted to Antje Forstroer for advice regarding analysis, to Jörg Geiger for advice regarding the multiple patch-clamp recording setup, and Michael Brecht and Rosanna Sammons for helpful comments on the manuscript.

Received: August 30, 2016

Revised: February 14, 2017

Accepted: April 13, 2017

Published: May 9, 2017

#### REFERENCES

- Bailu, S., Kropff, E., and Treves, A. (2012). Grid alignment in entorhinal cortex. *Biological Cybernetics* 106, 483–506.
- Barry, C., Hayman, R., Burgess, N., and Jeffery, K.J. (2007). Experience-dependent rescaling of entorhinal grids. *Nat. Neurosci.* 10, 682–684.
- Barry, C., Ginzberg, L.L., O'Keefe, J., and Burgess, N. (2012). Grid cell firing patterns signal environmental novelty by expansion. *Proc. Natl. Acad. Sci. USA* 109, 17687–17692.
- Barth, L., Burkhalter, A., Callaway, E.M., Connors, B.W., Cauli, B., DeFelipe, J., Feldmeyer, D., Freund, T., Kawaguchi, Y., Kisvarday, Z., et al. (2016). Comment on "Principles of connectivity among morphologically defined cell types in adult neocortex". *Science* 353, 1108.
- Beed, P., Bendels, M.H., Wiegand, H.F., Leibold, C., Johanning, F.W., and Schmitz, D. (2010). Analysis of excitatory microcircuitry in the medial entorhinal cortex reveals cell-type-specific differences. *Neuron* 68, 1059–1066.
- Boccaro, C.N., Sargolini, F., Thoresen, V.H., Solstad, T., Witter, M.P., Moser, E.I., and Moser, M.B. (2010). Grid cells in pre- and parasubiculum. *Nat. Neurosci.* 13, 987–994.
- Böhm, C., Peng, Y., Maier, N., Winterer, J., Poulet, J.F., Geiger, J.R., and Schmitz, D. (2015). Functional diversity of subicular principal cells during hippocampal ripples. *J. Neurosci.* 35, 13608–13618.
- Buetfering, C., Allen, K., and Monyer, H. (2014). Parvalbumin interneurons provide grid cell-driven recurrent inhibition in the medial entorhinal cortex. *Nat. Neurosci.* 17, 710–718.
- Burak, Y., and Fiete, I.R. (2009). Accurate path integration in continuous attractor network models of grid cells. *PLoS Comput. Biol.* 5, e1000291.
- Burgess, N., Barry, C., and O'Keefe, J. (2007). An oscillatory interference model of grid cell firing. *Hippocampus* 17, 801–812.
- Chen, G., Manson, D., Cacucci, F., and Wills, T.J. (2016). Absence of Visual Input Results in the Disruption of Grid Cell Firing in the Mouse. *Curr. Biol.* 26, 2335–2342.
- Couey, J.J., Witoelar, A., Zhang, S.J., Zheng, K., Ye, J., Dunn, B., Czajkowski, R., Moser, M.B., Moser, E.I., Roudi, Y., and Witter, M.P. (2013). Recurrent inhibitory circuitry as a mechanism for grid formation. *Nat. Neurosci.* 16, 318–324.
- Dhillon, A., and Jones, R.S. (2000). Laminar differences in recurrent excitatory transmission in the rat entorhinal cortex in vitro. *Neuroscience* 99, 413–422.
- Domnisoru, C., Kinkhabwala, A.A., and Tank, D.W. (2013). Membrane potential dynamics of grid cells. *Nature* 495, 199–204.
- Fuchs, E.C., Neitz, A., Pinna, R., Melzer, S., Caputi, A., and Monyer, H. (2016). Local and Distant Input Controlling Excitation in Layer II of the Medial Entorhinal Cortex. *Neuron* 89, 194–208.
- Fuhs, M.C., and Touretzky, D.S. (2006). A spin glass model of path integration in rat medial entorhinal cortex. *J. Neurosci.* 26, 4266–4276.
- Fyhn, M., Molden, S., Witter, M.P., Moser, E.I., and Moser, M.B. (2004). Spatial representation in the entorhinal cortex. *Science* 305, 1258–1264.
- Hafting, T., Fyhn, M., Molden, S., Moser, M.B., and Moser, E.I. (2005). Microstructure of a spatial map in the entorhinal cortex. *Nature* 436, 801–806.
- Heys, J.G., Rangarajan, K.V., and Dombeck, D.A. (2014). The functional microorganization of grid cells revealed by cellular-resolution imaging. *Neuron* 84, 1079–1090.
- Jouhanneau, J.S., Kremkow, J., Dorm, A.L., and Poulet, J.F. (2015). In Vivo Monosynaptic Excitatory Transmission between Layer 2 Cortical Pyramidal Neurons. *Cell Rep.* 13, 2098–2106.
- Kropff, E., and Treves, A. (2008). The emergence of grid cells: Intelligent design or just adaptation? *Hippocampus* 18, 1256–1269.
- McNaughton, B.L., Battaglia, F.P., Jensen, O., Moser, E.I., and Moser, M.B. (2006). Path integration and the neural basis of the 'cognitive map'. *Nat. Rev. Neurosci.* 7, 663–678.
- Moser, E.I., Roudi, Y., Witter, M.P., Kentros, C., Bonhoeffer, T., and Moser, M.B. (2014). Grid cells and cortical representation. *Nat. Rev. Neurosci.* 15, 466–481.
- Pastoll, H., Solanka, L., van Rossum, M.C., and Nolan, M.F. (2013). Feedback inhibition enables  $\theta$ -nested  $\gamma$  oscillations and grid firing fields. *Neuron* 77, 141–154.
- Peng, Y., Barreda Tomás, F.J., Klisch, C., Vida, I., and Geiger, J.R.P. (2017). Layer-Specific Organization of Local Excitatory and Inhibitory Synaptic Connectivity in the Rat Presubiculum. *Cereb. Cortex* 27, 2435–2452.
- Pérez-Escobar, J.A., Kornienko, O., Latuske, P., Kohler, L., and Allen, K. (2016). Visual landmarks sharpen grid cell metric and confer context specificity to neurons of the medial entorhinal cortex. *eLife* 5, e16937.
- Quilichini, P., Sirota, A., and Buzsáki, G. (2010). Intrinsic circuit organization and theta-gamma oscillation dynamics in the entorhinal cortex of the rat. *J. Neurosci.* 30, 11128–11142.
- Rowland, D.C., Roudi, Y., Moser, M.B., and Moser, E.I. (2016). Ten Years of Grid Cells. *Annu. Rev. Neurosci.* 39, 19–40.
- Schmidt-Hieber, C., and Häusser, M. (2013). Cellular mechanisms of spatial navigation in the medial entorhinal cortex. *Nat. Neurosci.* 16, 325–331.
- Sun, C., Kitamura, T., Yamamoto, J., Martin, J., Pignatelli, M., Kitch, L.J., Schnitzer, M.J., and Tonegawa, S. (2015). Distinct speed dependence of entorhinal island and ocean cells, including respective grid cells. *Proc. Natl. Acad. Sci. USA* 112, 9466–9471.

- Tang, Q., Ebbesen, C.L., Sanguinetti-Scheck, J.I., Preston-Ferrer, P., Gundl-finger, A., Winterer, J., Beed, P., Ray, S., Naumann, R., Schmitz, D., et al. (2015). Anatomical Organization and Spatiotemporal Firing Patterns of Layer 3 Neurons in the Rat Medial Entorhinal Cortex. *J. Neurosci.* *35*, 12346–12354.
- Tocker, G., Barak, O., and Derdikman, D. (2015). Grid cells correlation structure suggests organized feedforward projections into superficial layers of the medial entorhinal cortex. *Hippocampus* *25*, 1599–1613.
- Turing, A.M. (1952). The chemical basis of morphogenesis. *Philos. Trans. R. Soc. Lond. B Biol. Sci.* *237*, 37–72.
- Varga, C., Lee, S.Y., and Soltesz, I. (2010). Target-selective GABAergic control of entorhinal cortex output. *Nat. Neurosci.* *13*, 822–824.
- Yoon, K., Buice, M.A., Barry, C., Hayman, R., Burgess, N., and Fiete, I.R. (2013). Specific evidence of low-dimensional continuous attractor dynamics in grid cells. *Nat. Neurosci.* *16*, 1077–1084.

**Cell Reports, Volume 19**

**Supplemental Information**

**Excitatory Microcircuits within Superficial**

**Layers of the Medial Entorhinal Cortex**

**Jochen Winterer, Nikolaus Maier, Christian Wozny, Prateep Beed, Jörg Breustedt, Roberta Evangelista, Yangfan Peng, Tiziano D'Albis, Richard Kempter, and Dietmar Schmitz**

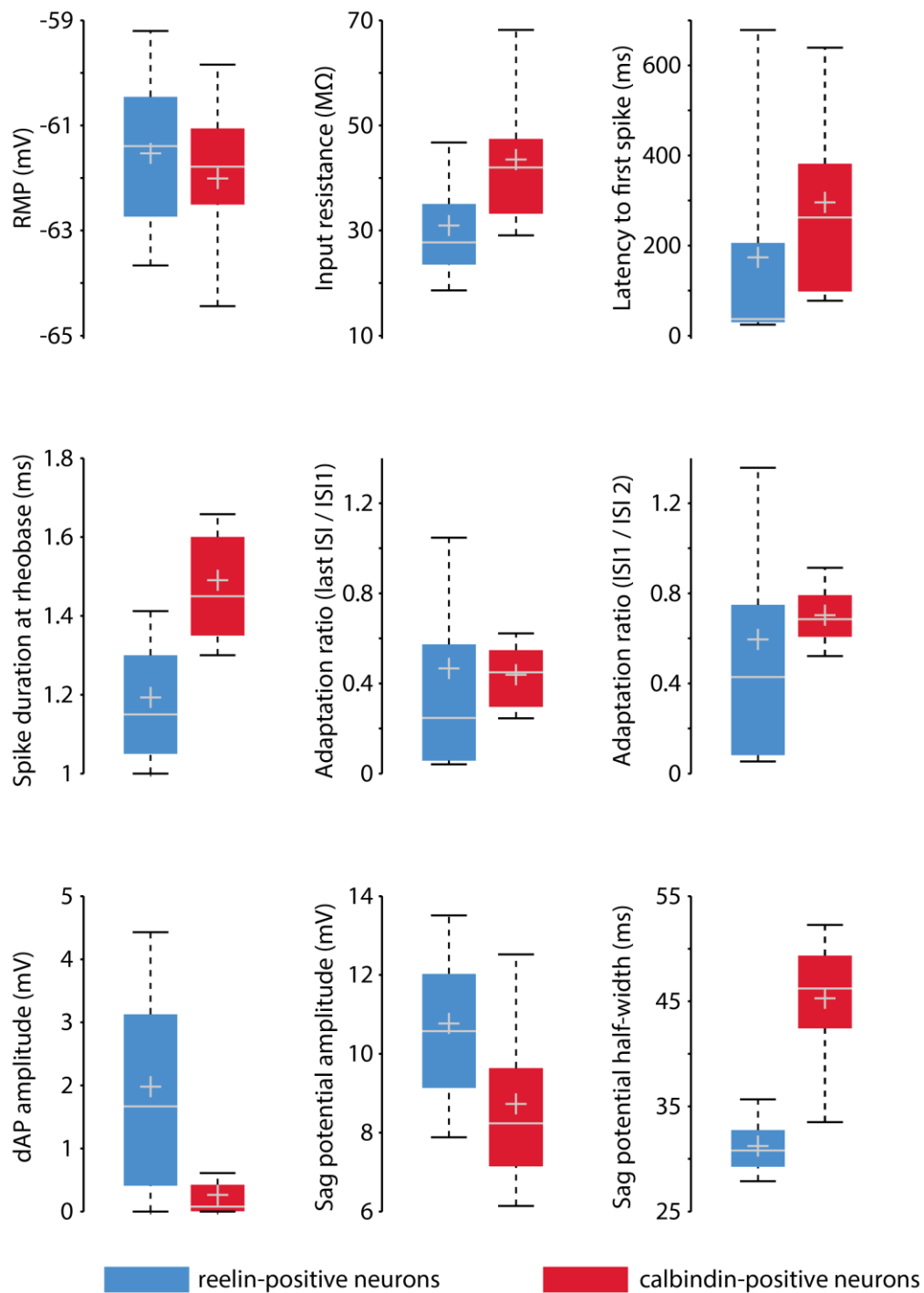


**Figure S1. Intrinsic properties of reelin-positive and calbindin-positive cells in layer II of the entorhinal cortex, Related to Figure 1.** Included are successfully stained cells, for which all nine intrinsic electrophysiological properties were recorded ( $n = 115$  reelin-positive cells, blue, and  $n = 26$  calbindin-positive cells, red). For details concerning the analysis of the respective parameter see **Supplemental Experimental Procedures** below. Box edges indicate the first and third quartiles, the median and the mean are given by the grey line and ‘plus’ symbols, respectively. Percentages spanned by the whiskers correspond to 9% and 91%, respectively.

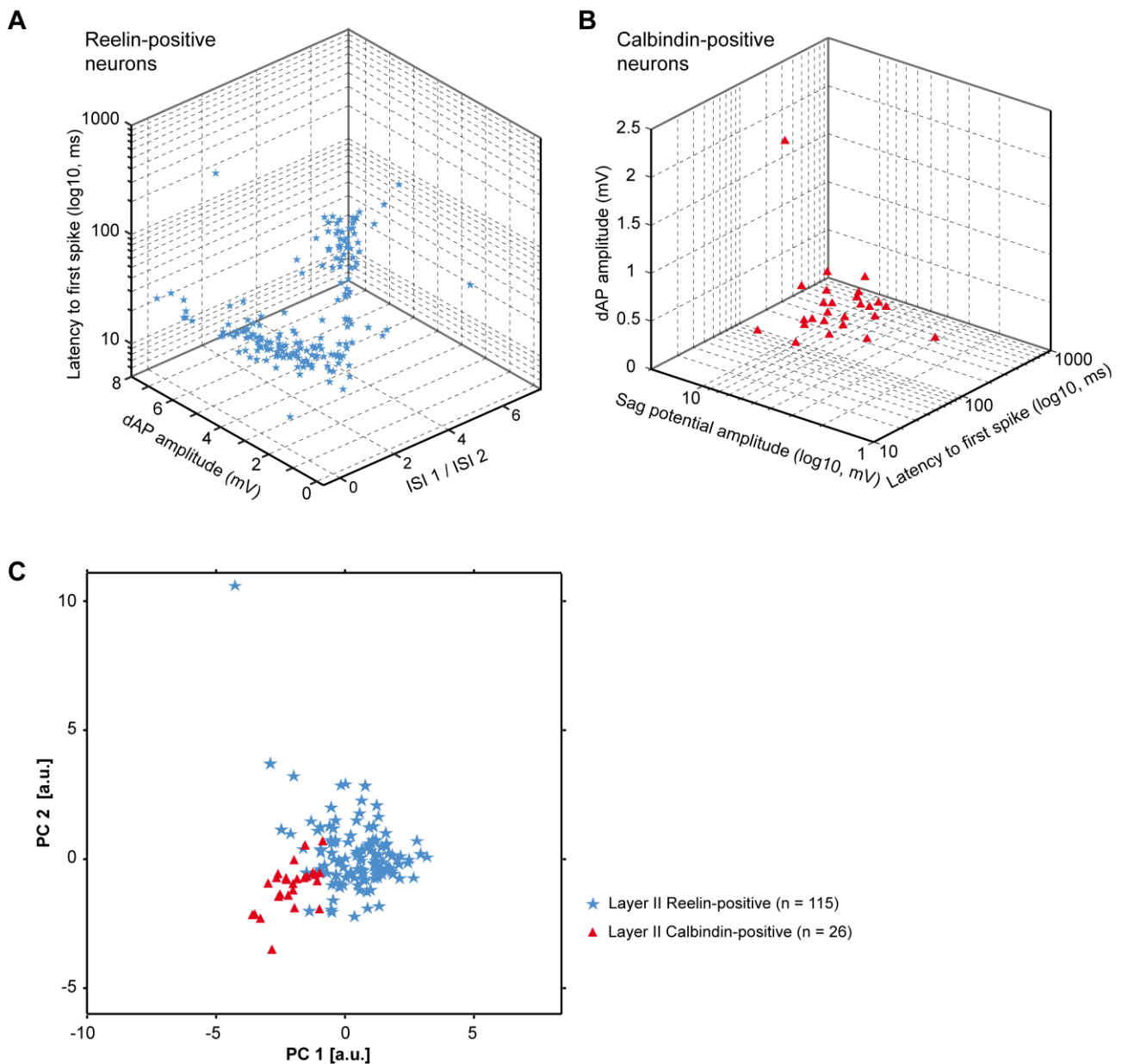


**Figure S2. Absence of further categorization among reelin- and calbindin-expressing principal neurons in layer II of the MEC, Related to Figure 1.** (A) For layer II stellate cells (n = 180) the distribution of three intrinsic parameters is plotted (as in Fuchs et al., 2016): the depolarizing afterpotential (dAP) amplitude, the latency to first spike, and the ratio of interspike interval 1 and interspike interval 2 (ISI 1 / ISI 2). Based on these criteria no further categorization of stellate cells was detected. (B) Similarly, the distribution of three intrinsic parameters in 27 identified (calbindin-expressing) layer II pyramidal neurons: depolarizing afterpotential (dAP) amplitude, latency to first spike, and sag potential amplitude, as in Fuchs et al., 2016. Based on these criteria, no further categorization of stellate cells was observed. (C) Principal component analysis performed on all nine intrinsic electrophysiological parameters. The projection on the first two principal components shows a clear separation between the two classes. Included are successfully stained cells for which all nine intrinsic electrophysiological properties were recorded (see also Figure S1 for display of all parameters).

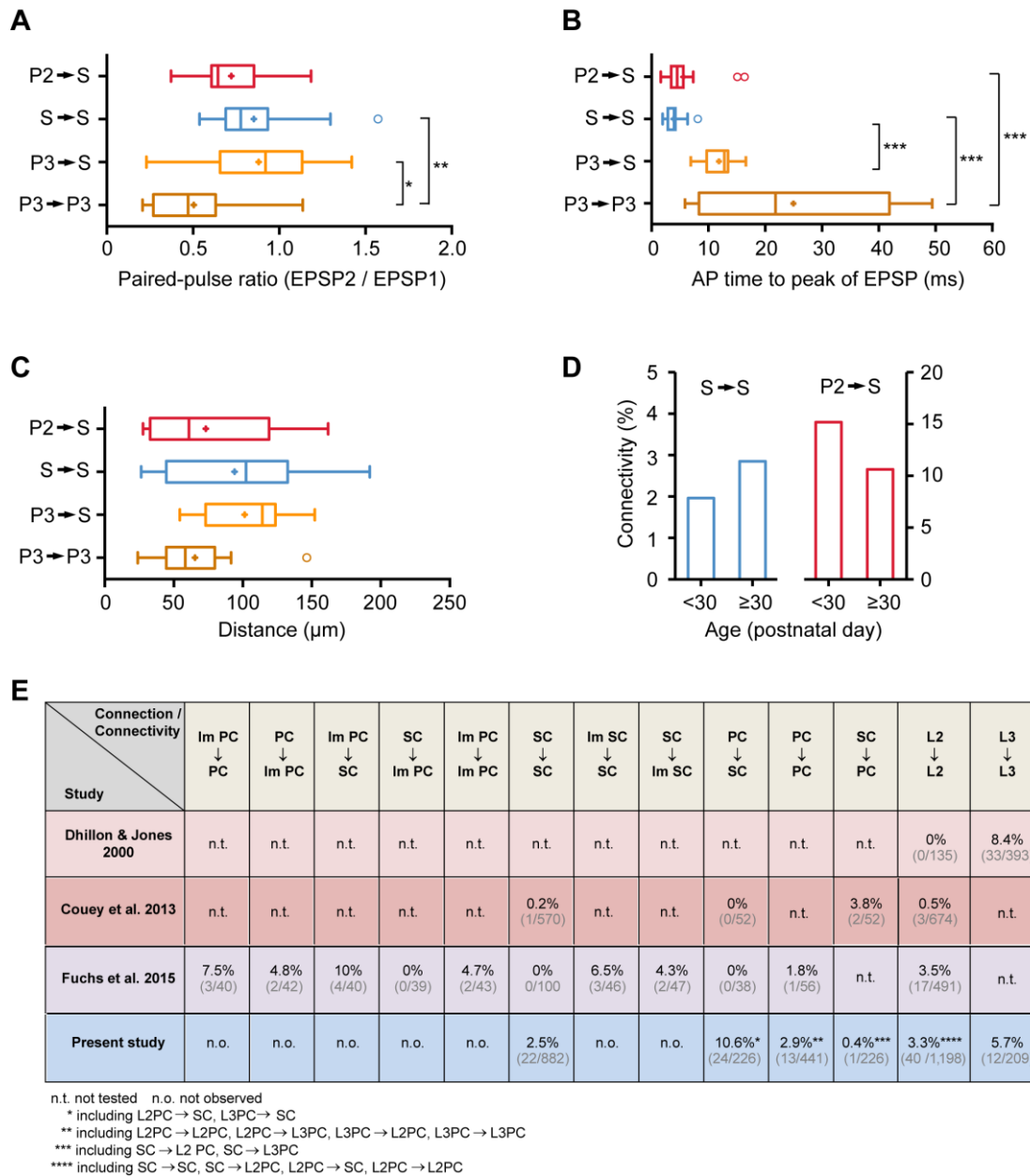


**Figure S3. Properties of excitatory synaptic connections in the superficial layers of the MEC, Related to Figure 4.** (A) Paired-pulse ratios (EPSP2/EPSP1) for the different groups. (B) AP time to peak for the different groups, measured as time from the peak of the presynaptic AP to the peak of the postsynaptic EPSP. (C) Distance of the connected cells, measured from the centers of the somata. (D) Connection probability between stellate cell – stellate cell (S→S) and layer II pyramidal cell – stellate cell (P2→S) at different ages. Age range from p21 to p29: (S→S) 2.0% (seven out of 356 connections tested) and (P2→S) 15.2% (12 out of 79 connections tested). Age range from p30 to p60: (S→S) 2.9% (15 out of 526 connections tested) and (P2→S) 10.6% (five out of 47 connections tested). Statistical significance of displayed differences was assessed by Dunn’s test of multiple comparisons. \*  $P \leq 0.05$ ; \*\*  $P \leq 0.01$ ; \*\*\*  $P \leq 0.001$ ; \*\*\*\*  $P \leq 0.0001$ . Properties are shown only for contacts with more than one connection found. (E) Compilation of excitatory connectivity values in superficial layers of MEC based on previous studies. Numbers are gathered from Dhillon and Jones (2000), Couey et al. (2013) and Fuchs et al. (2015), and the present study. *Abbreviations:* SC: Stellate cell, Im SC: intermediate stellate cells, PC: pyramidal cells, Im PC: intermediate pyramidal cells, L2: layer II principal cells, L3: layer III pyramidal cells.

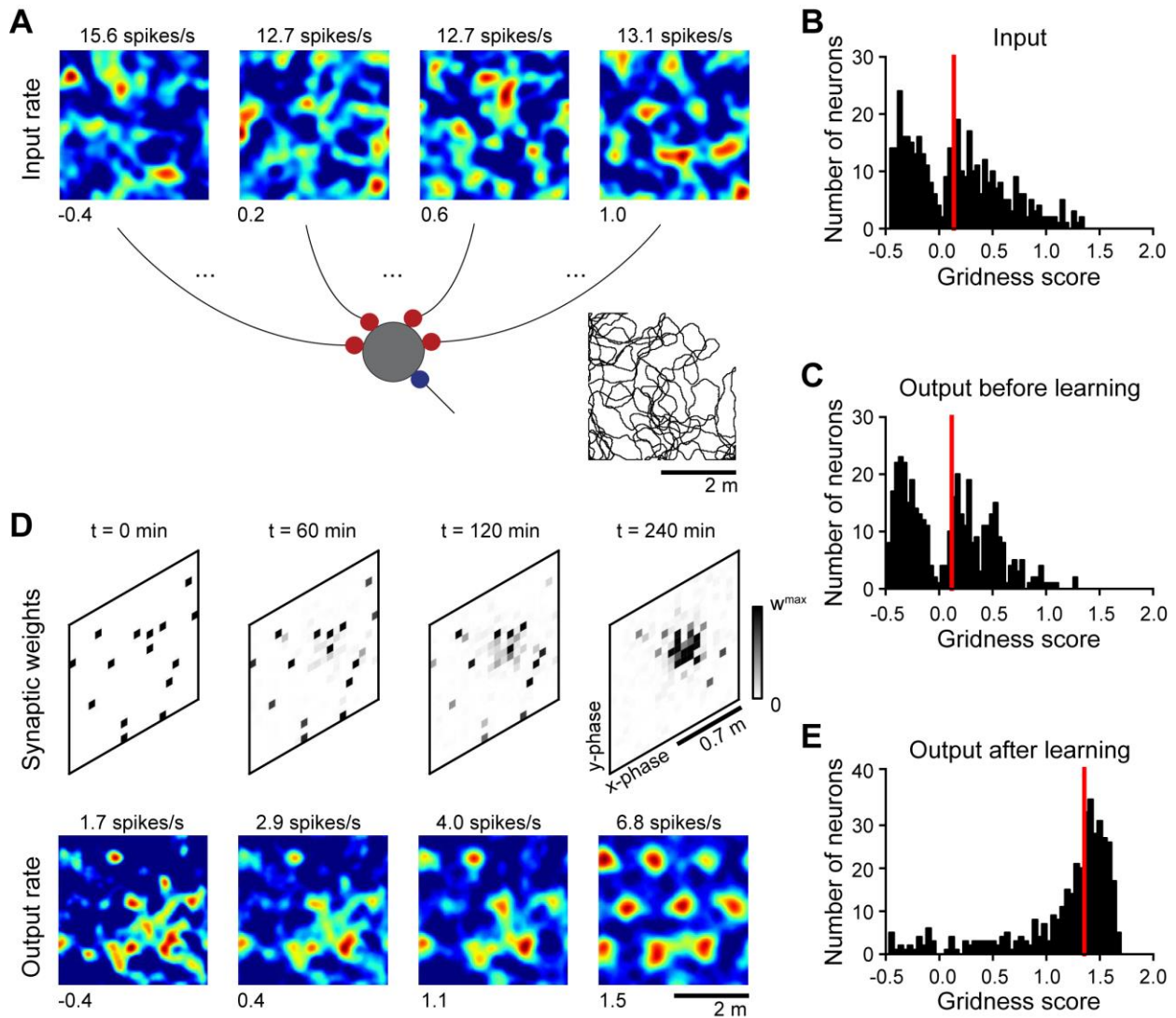


**Figure S4. Improvement of grid tuning in a feed-forward network model, Related to Figure 4.** (A) Model schematic. In a target principal-cell population, each output neuron (example: grey disc) receives feed-forward excitation (red discs) from  $N^{in}$  spatially tuned inputs and inhibition (blue disc) from spatially-untuned interneurons. At the top row, four examples of the input rate maps are shown (dark blue: 0 spikes/s, dark red: peak rate reported at the top, gridness score reported at the bottom left corner). Input rate maps are noisy hexagonal grids with common spacing and orientation but different phases. An example of the trajectory covered by a virtual-rat is shown at the bottom right (10 minutes of exploration). (B) Gridness scores of the excitatory inputs ( $N^{in} = 400$ , see examples in A). (C) Gridness scores of the outputs before learning, i.e., with random feed-forward weights ( $N^{out} = 400$ ). (D) Development of the excitatory synaptic weights (top row, weights from 0 to  $w^{max}$  in grey scale) and corresponding output firing rate maps (bottom row) for one example output neuron. Four snapshots are shown (see simulation times at the top). Nearby pixels in the synaptic weight maps correspond to inputs with similar grid phases. Output rates are color-coded as in A. (E) Gridness scores of the outputs at the end of the simulation ( $t = 240$  min). The red vertical lines in B, C, and E denote median gridness score values.

## Supplemental Experimental Procedures

*Cell classification.* To differentiate layer II principal neurons, we made use of the differential immunoreactivity of these cells, i.e. stellate cells expressing the glycoprotein reelin and pyramidal neurons expressing the Ca<sup>2+</sup> binding protein calbindin (Varga et al., 2010). Immunolabeling revealed 238 reelin-positive and 48 calbindin-positive cells, enabling us to classify them as stellate- and pyramidal neurons, respectively. We further analyzed nine electrophysiological parameters in all cells, if possible (Figure S1; see also Alonso and Klink, 1993; Canto and Witter, 2012): *Resting membrane potential* values represent initial voltages recorded after arriving in the whole-cell configuration. The *input resistance* was calculated from the deviation from baseline of steady-state voltage responses evoked by intracellular current injections (50 pA). The *latency to first spike* at rheobase was determined as the time from the onset of the depolarization step current to the onset of the action potential (threshold:  $dV/dt \geq 90$  V/s). The *spike duration at rheobase* was found as the duration from spike onset to the time point where the decaying slope of the action potential crossed the onset voltage level again. The *adaptation ratio* was calculated both as the ratio of the last and the first interspike intervals (last ISI / ISI 1) or as the ratio of the first two interspike intervals (ISI 1 / ISI 2) at current steps of +500 pA and 1000 ms. The *depolarizing afterpotential (dAP)* for spikes at rheobase was determined by calculating the voltage difference between the local minimum of the fast afterhyperpolarization (fAHP) and the following depolarizing peak (Alonso and Klink, 1993). *Amplitude and half-width* (i.e., the duration at 50% of the amplitude) of the *sag potential* were measured in response to -750 pA (or -100 pA) current injection. We observed that the half-width of the sag potential -750 pA current injection predicted best the immunoreactivity to reelin and calbindin of layer II principal cells (Fig. S1). This enabled us to define a threshold for the classification of cells with non-sufficient staining. To find the best separation value, we used a linear 1d support vector machine (SVM, from the Python scikit-learn package, version 0.18.1) taking into account the class imbalance of reelin-positive and calbindin-positive cell numbers. The weighted SVM for the half-width of the sag potential was 37.2 ms (accuracy: 0.93; 10-fold cross validation) at -750 pA current injection (in some of the recorded cells we injected only -100 pA, yielding a weighted SVM of 45.2 ms with a slightly reduced accuracy: 0.85; 10-fold cross validation). Finally, we classified neurons that were non-sufficiently stained as follows: cells were classified as reelin-positive and therefore as stellate cells, if the half-width of the sag potential was  $\leq 36$  ms for -750 pA current injection (or  $\leq 42$  ms for -100 pA current injection) and as calbindin-positive and therefore as pyramidal cells if the half-width of the sag potential was  $\geq 38$  ms (-750 pA) or  $\geq 48$  ms (-100 pA). Layer III pyramidal cells could be easily distinguished from both layer II pyramidal and stellate cells based on clear differences in input resistance (mean  $\pm$  SD:  $124 \pm 32$  M $\Omega$ ) and resting membrane potential (mean  $\pm$  SD:  $-67 \pm 5$

mV) in layer III pyramidal cells (see Fig. S1 for comparison with layer II stellate and pyramidal neurons).

*Modeling.* Here we show that feed-forward excitatory projections could support the inheritance of grid-cell activity across distinct neuronal populations, and that grid patterns could become more regular through this inheritance process. To this end, we model the activity of a population of weakly-tuned grid cells projecting to a target principal-cell population as a virtual rat explores a square enclosure. Input firing-rate maps were obtained by distorting with noise hexagonal grids with common spacing and orientation, but different spatial phases (Fig. S4A, B), similarly to what is observed within a grid-cell module (Hafting et al., 2005). The feed-forward connectivity was sparse and initially random, that is, each neuron in the target principal-cell population received input from a set of noisy grids with random spatial phases. Such a random connectivity slightly decreased the grid tuning of the output spatial maps (Fig. S4C). Indeed, in a feed-forward network, the output grid tuning could be improved only by selecting input grids with similar phases. But how to obtain such an input selection that crucially depends on the behavioral correlates of neural activity?

We suggest that Hebbian plasticity could drive this selection. In Fig. S4D we illustrate this hypothesis for one example output neuron in the target principal-cell population. Initially, the output neuron was driven by a random set of inputs, and the corresponding output firing-rate map was spatially irregular (Fig. S4D, left-most panels). With experience, however, inputs with similar grid phases increased their synaptic strength, and, as a result, a more regular grid pattern emerged at the output (Fig. S4D, right-most panels). The spatial phase of the output grid depended on the initial state of the synaptic weights and on the trajectory of the virtual rat, which were both random. Nevertheless, regardless of the initial conditions, the firing-rate maps at the output (Fig. S4E) were consistently more regular than the ones at the input (Fig. S4B).

In summary, we demonstrate with a computational model that grid tuning could be inherited and even be improved via feed-forward projections across distinct principal-cell populations. We assumed that the experimentally observed feed-forward connections (Figs. 1-3) were also representative for grid cells and that cells with weak grid tuning (same period, same orientation, but different phase) in an input layer projected to a target grid cell in an output layer. Note that inheritance requires only weak grid tuning at the input layer (see input gridness scores in Fig. S4B).

A connectivity pattern suitable for the inheritance was learned from the activity correlations already present at the input. We suggest that such learning could happen concurrently with the development of grid cells in the first ~3 weeks of age (Langston et al., 2010; Wills et al., 2012, 2010), and that grid-field inheritance could take place in feed-forward projections from pyramidal cells in layer II or III to stellate cells in layer II. This is in line with recent reports that both stellate and pyramidal cells

show grid spatial tuning (Sun et al., 2015), although it remains unclear which principal-cell population contains the most-regular grids (Sun et al., 2015; Tang et al., 2014).

*Model implementation.*

We model a feed-forward network of  $N^{\text{in}}$  excitatory inputs with rates  $\{r_j^{\text{in}} : j = 1, 2, \dots, N^{\text{in}}\}$  projecting to  $N^{\text{out}}$  excitatory outputs with rates  $\{r_i^{\text{out}} : i = 1, 2, \dots, N^{\text{out}}\}$ , where

$$r_i^{\text{out}}(\vec{x}) = \left[ \sum_{j=1}^{N^{\text{in}}} w_{ij} r_j^{\text{in}}(\vec{x}) - r_0 \right]_+ . \quad (1)$$

The vector  $\vec{x} = [x_1, x_2]$  is the position of the virtual rat in the environment,  $w_{ij}$  is the synaptic weight from input neuron  $j$  to output neuron  $i$ ,  $r_0 > 0$  spikes/s is a spatially-homogeneous inhibitory rate, and the function  $[z]_+ = z$  if  $z > 0$ ,  $= 0$  if  $z \leq 0$  is a static non-linearity. The input rates are modeled by distorting with noise hexagonal grids with common spacing and orientation, but different spatial phases:

$$r_j^{\text{in}}(\vec{x}) = \left[ a g_j(\vec{x}) + (1 - a) \xi_j(\vec{x}) \right]_+ , \quad (2)$$

where  $g_j(\vec{x})$  is a hexagonal grid with phase  $\vec{\varphi}_j$ ,  $\xi_j(\vec{x})$  is a realization of a 2-dimensional noise process, and the parameter  $0 < a < 1$  weights the strength of the grid signal in relation to the noise. The grid signal  $g_j(\vec{x})$  is the sum of three planar waves with wave vectors  $\{\vec{k}_n : n = 0, 1, 2\}$  that are 60 degrees apart:

$$g_j(\vec{x}) = B \left[ \sum_{n=0}^{n=2} \cos(\vec{k}_n \cdot (\vec{x} + \vec{\varphi}_j)) \right]_+ \quad \text{with} \quad \vec{k}_n = \frac{4\pi}{T\sqrt{3}} \begin{bmatrix} \cos(n\pi/3 + \beta) \\ \sin(n\pi/3 + \beta) \end{bmatrix} , \quad (3)$$

where  $B > 0$  controls the grid amplitude,  $\beta$  sets the grid orientation, and  $T$  is the grid spacing. The spatial phases  $\{\vec{\varphi}_j\}$  are sampled to cover the entire phase space evenly. The input noise is uncorrelated across neurons but correlated across spatial locations such that it varies smoothly in space. Specifically, the noise is generated by low-pass filtering 2-dimensional white Gaussian noise with a circularly-symmetric Gaussian filter:  $G(\vec{x}) = \exp(-|\vec{x}|/2\sigma_x^2)$ , where  $\sigma_x$  controls the filter width. The mean and the variance of the noise are normalized to match the ones of the input signal  $g_j(\vec{x})$ .

The excitatory synaptic weights  $\{w_{ij}\}$  are changed according to the following Hebbian learning rule:

$$\frac{dw_{ij}}{dt} = \eta(r_j^{\text{in}} - \gamma)r_i^{\text{out}}, \quad (4)$$

where  $\eta$  is a small learning rate and  $\gamma > 0$  spikes/s sets the threshold between long-term potentiation and long-term depression. Additionally, the synaptic weights  $\{w_{ij}\}$  are bounded between 0 and  $w^{\text{max}}$  at each time point. At the initial condition, a random subset of  $N^{\text{up}} < N^{\text{in}}$  synaptic weights are set at the upper bound  $w^{\text{max}} > 0$  whereas all the other weights are set to 0.

The virtual rat explores a square arena of side-length  $L$  with a correlated random walk with movement directions that vary smoothly in time. Precisely, the rat's trajectory is a sample of the 2-dimensional stochastic process

$$\frac{d\vec{X}_t}{dt} = v [\cos(\theta_t), \sin(\theta_t)] \quad \text{with} \quad \theta_t = \sigma_\theta W_t, \quad (5)$$

where  $\vec{X}_t$  is the position of the virtual rat at time  $t$ , the process  $\theta_t$  sets the direction of motion, and  $W_t$  is a standard Wiener process. The parameters  $v$  and  $\sigma_\theta$  control the speed of motion and the tortuosity of the trajectory. At the boundaries of the environment, only movement directions towards the interior of the arena are retained.

Parameter values:  $N^{\text{in}} = N^{\text{out}} = 400$ ,  $r_0 = 3$  spikes/s,  $a = 0.27$ ,  $B = 6$ ,  $\beta = 0$ ,  $T = 1.4$  m,  $\sigma_x = 0.15$  m,  $\eta = 2 \cdot 10^{-5}$  1/s,  $\gamma = 3.8$  spikes/s,  $w^{\text{max}} = 0.067$ ,  $N^{\text{up}} = 15$ ,  $L = 4$  m,  $v = 0.2$  m/s,  $\sigma_\theta = 0.7$ .

Gridness scores of input and output firing-rate maps were computed with the algorithm proposed by (Stensola et al., 2012).

## Supplemental References

- Alonso, A., Klink, R. (1993). Differential electroresponsiveness of stellate and pyramidal-like cells of medial entorhinal cortex layer II. *J. Neurophysiol.* *70*, 128–143.
- Canto, C.B., Witter, M.P. (2012). Cellular properties of principal neurons in the rat entorhinal cortex. II. The medial entorhinal cortex. *Hippocampus* *22*, 1277–1299.
- Hafting, T., Fyhn, M., Molden, S., Moser, M., Moser, E.I. (2005). Microstructure of a spatial map in the entorhinal cortex. *Nature* *436*, 801–806.
- Langston, R.F., Ainge, J.A., Couey, J.J., Canto, C.B., Bjerknes, T.L., Witter, M.P., Moser, E.I., Moser, M.-B. (2010). Development of the Spatial Representation System in the Rat. *Science* *328*, 1576–1581.
- Stensola, H., Stensola, T., Solstad, T., Frøland, K., Moser, M.-B., Moser, E.I. (2012). The entorhinal grid map is discretized. *Nature* *492*, 72–8.
- Sun, C., Kitamura, T., Yamamoto, J., Martin, J., Pignatelli, M., Kitch, L.J., Schnitzer, M.J., Tonegawa, S. (2015). Distinct speed dependence of entorhinal island and ocean cells, including respective grid cells. *Proc. Natl. Acad. Sci.* *112*, 9466–9471.
- Tang, Q., Burgalossi, A., Ebbesen, C.L., Ray, S., Naumann, R., Schmidt, H., Spicher, D., Brecht, M. (2014). Pyramidal and stellate cell specificity of grid and border representations in layer 2 of medial entorhinal cortex. *Neuron* *84*, 1191–1197.
- Varga, C., Lee, S.Y., Soltesz, I. (2010). Target-selective GABAergic control of entorhinal cortex output. *Nat. Neurosci.* *13*, 822–4.
- Wills, T.J., Barry, C., Cacucci, F. (2012). The abrupt development of adult-like grid cell firing in the medial entorhinal cortex. *Front. Neural Circuits* *6*, 21. doi: 10.3389.
- Wills, T.J., Cacucci, F., Burgess, N., O’Keefe, J. (2010). Development of the hippocampal cognitive map in preweanling rats. *Science* *328*, 1573–1576.